Electronic Supplementary Material (ESI) for Physical Chemistry Chemical Physics.

Supplementary Information for

Transparent grating-based metamaterials for dynamic infrared radiative regulation smart windows

Pan Wang[1,2], Haoyu Wang[1,2], Ya Sun[1,2], Mengqi Zhang[1,2], Shaowen Chen[1,2], Chengyu Xiao[1,2], and Han Zhou[1,2]✉

[1]State Key Laboratory of Metal Matrix Composites, School of Materials Science and Engineering, Shanghai Jiao Tong University, Shanghai 200240, P. R. China.
[2]Future Materials Innovation Center, Zhangjiang Institute for Advanced Study, Shanghai Jiao Tong University, Shanghai 201203, P. R. China.
✉e-mail: hanzhou_81@sjtu.edu.cn

Contents Summary:

Supplementary Notes 1-4

Supplementary Figures 1-11

Supplementary Notes

Supplementary Note 1. Optical performance simulations of ITO grating-based metamaterials.

We conducted the Lumerical FDTD solutions to determine the optical properties of IDIR in the wavelength range of 0.3-30 μm. Periodic boundary conditions and perfectly matched layers were set in the x-y and z directions in the simulation regions, respectively. A vertically incident plane wave source was directed toward the surface of the models in the z-direction. We used movie monitors to capture the time-domain electric field of IR light interaction with the IDIR in both the high and low ε states.

Supplementary Note 2. Calculation of the IR spectra with different permittivities

In the proposed device structure and actuation methods, the thickness of the insulator layer can be tuned by electrical bias. The permittivity dispersion of ITO could also be partly tuned by electrical bias due to electron doping[1]. As mentioned before, ITO behaves metal-like in the IR, and therefore, we can employ the Drude free-electron model for the dielectric permittivities at the wavelengths of 3-30 μm. ω_p is the plasma frequency which is related to the carrier density N and electron effective mass m^* as $\omega_p^2 = Ne^2/(\varepsilon_0 m^*)$[1, 2]. e is the electron charge. According to the Drude free-electron model, when the carrier density N increases, the real part of the permittivity will decrease but the imaginary part will increase. In addition, carrier density N likewise increased with the electrical bias due to the electron injection. Therefore, when applying an electrical bias to ITO, the permittivity's real part will decrease and the imaginary part will increase.

For our proposed dynamic IR radiation regulator, before actuation ($d > 0$), the regulator with the F-P cavity shows a high ε. When applying an electrical bias, the generated force drives the ITO grating toward the ITO reflector and the F-P cavity disappears ($d = 0$) meanwhile switching to the low ε state. Thus, electrical bias will not influence the F-P cavity in the high ε state. However, it will affect the permittivity values and IR spectra in the low ε state. As it is difficult to obtain exact permittivity values under different electrical biases, to simplify the calculation, we assumed dielectric permittivity's real (imaginary) part decreased (increased) by 0%, 10%, 20%, 30%, and 40%. The results show that the decreased permittivity's real part and the increased imaginary part will lead to a slight decrease in the ε value but a slight increase in the $\triangle\varepsilon$ (Fig. S3).

Supplementary Note 3. Calculation of the integrated solar irradiance absorptance

The energy of solar radiation (AM1.5G) is mainly concentrated in the wavelength range of 0.25~2.5 μm, with the energy proportions of the UV (0.25-0.38 μm), VIS (0.38-0.78 μm), and NIR (0.78-2.5 μm) being 3.3%, 53.1%, and 43.6%, respectively. The energy is a nonuniform distribution across the total solar spectrum. Therefore, the integrated solar irradiance absorptance is used to provide a more accurate evaluation of the performance in solar spectrum ranges. The integrated solar irradiance absorptance α_{sun} of the device can be given by[3]

$$\alpha_{sun} = \frac{\int \alpha(\lambda)\Psi(\lambda)d\lambda}{\int \alpha\Psi(\lambda)d\lambda} \quad (1)$$

where $\alpha(\lambda)$ is the absorptance at a wavelength of λ, and $\Psi(\lambda)$ is the solar irradiance at 1.5 air mass.

Supplementary Note 4. Calculation of the thermal IR radiation tunability

Under thermal equilibrium conditions, Kirchhoff's law depicts that the emissivity at wavelength λ equals the absorptivity in the same wavelength.

The ε of the IDIR regulator can be calculated by

$$\varepsilon(\lambda) = 1 - R(\lambda) - T(\lambda) \quad (1)$$

where R and T are the IR reflectivity and the transmittance of the device, respectively.

The dynamic tuning power ΔP of such a device can be obtained by:

$$\Delta P = P_{net}^{\varepsilon_{high}} - P_{net}^{\varepsilon_{low}} \quad (2)$$

where $P_{net}^{\varepsilon_{high}}$ and $P_{net}^{\varepsilon_{low}}$ are the net radiation power (P_{net}) of the device in the high emissivity (ε_{high}) and low emissivity (ε_{low}) states, respectively. And the P_{net}, the absorbed solar radiation (P_{sun}), the radiative heat from the device (P_{cool}), the heat radiation absorbed from the atmosphere (P_{atm}), and the nonradiative power lost due to convection and conduction (P_{non}) can be expressed by the following equations:

$$P_{net}(T_{dev}, T_{amb}) = P_{cool}(T_{dev}) - P_{sun} - P_{atm}(T_{amb}) - P_{non}(T_{dev}, T_{amb}) \quad (3)$$

$$P_{cool}(T_{dev}) = A_{dev}\int d\Omega cos\theta \int_0^\infty d\lambda I_{BB}(T_{dev},\lambda)\varepsilon_{dev}(\lambda,\theta) \quad (4)$$

$$P_{sun}(T_{dev}) = A_{dev}cos\theta_{sun}\int_0^\infty d\lambda I_{sun}(\lambda)\varepsilon_{dev}(\lambda,\theta_{sun}) \quad (5)$$

$$P_{atm}(T_{amb}) = A_{dev}\int d\Omega cos\theta \int_0^\infty d\lambda I_{BB}(T_{amb},\lambda)\varepsilon_{dev}(\lambda,\theta)\varepsilon_{atm}(\lambda,\theta) \quad (6)$$

$$P_{non}(T_{dev}, T_{amb}) = A_{dev}h_c(T_{amb} - T_{dev}) \quad (7)$$

Here, A_{dev} is the area of the device. $I_{BB}(T,\lambda)$ is the spectral power density of the blackbody at temperature T. I_{sun} is the incident solar power absorbed by the device.

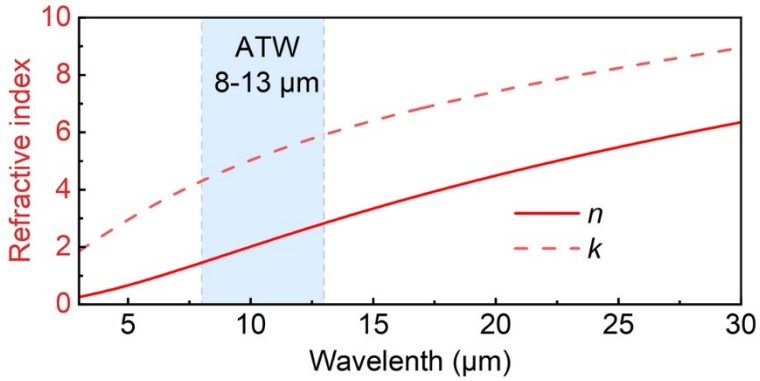

Fig. S1. Complex refractive index of ITO in 3-30 μm. The real (*n*) and imaginary parts (*k*) are determined by $\epsilon = n^2 - k^2 + 2nki$.

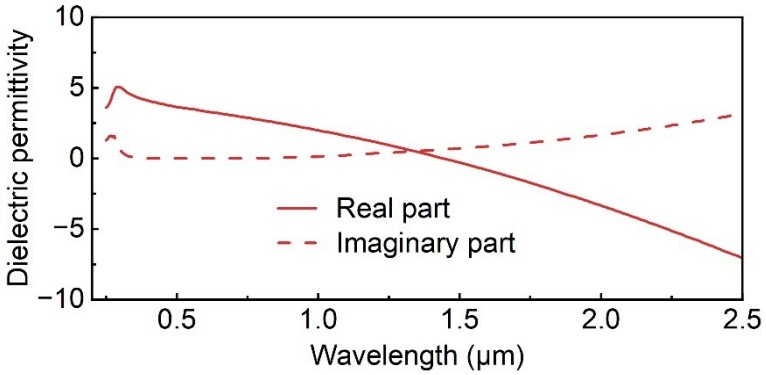

Fig. S2. Complex dielectric permittivity of ITO at 0.25-2.5 μm. The data are adapted from reported reference based on ITO film samples annealed in an oven at 350 °C for 1 h in N_2[4].

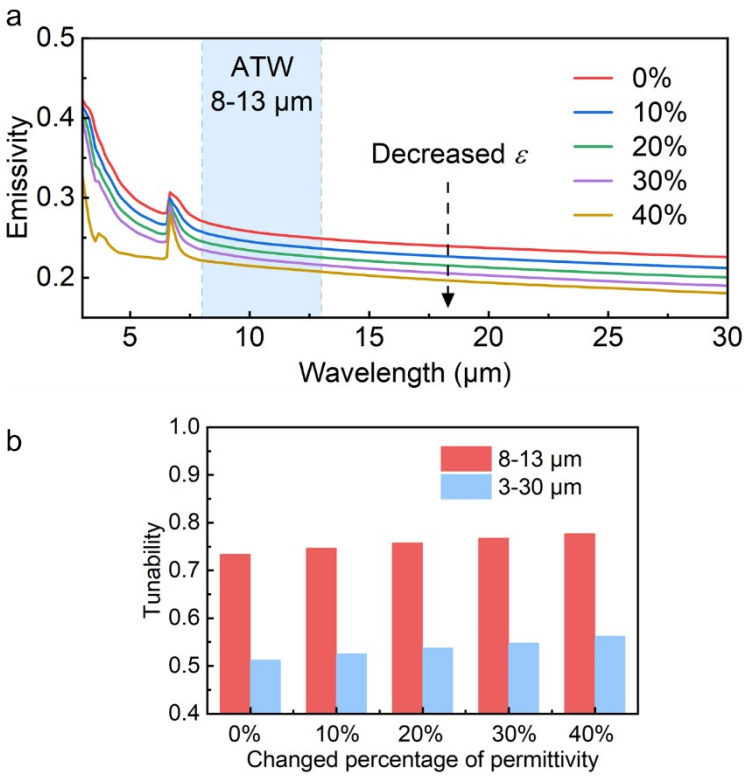

Fig. S3. (a) The spectral performance in the low ε state with different dielectric permittivity real (imaginary) part reductions (increment) of 0%, 10%, 20%, 30%, and 40%. (b) Tunability of the devices with different dielectric permittivity. The results show that the decreased permittivity real part and the increased imaginary part will lead to a decrease in the ε value and a slight increase in the $\triangle\varepsilon$.

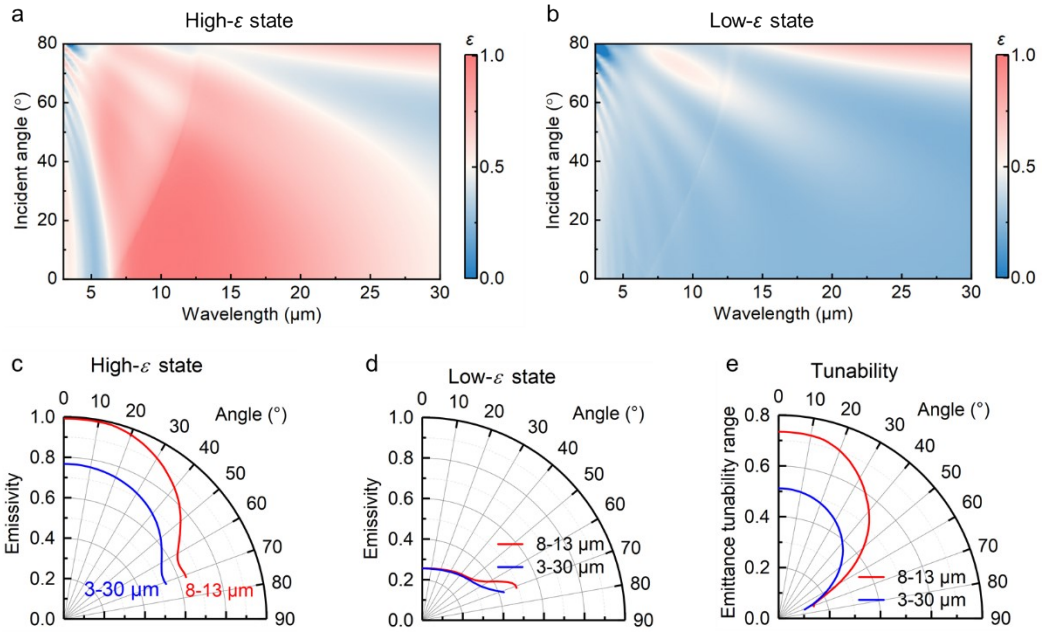

Fig. S4. Angle dependence of the spectral performance in the (a) high and (b) low ***ε*** states. Average ***ε*** of the IDIR regulator varying with the angle of incidence in (c) high and (d) low ***ε*** states. (e) The tunability ***△ε of*** the IDIR regulator varying with the angle of incidence. The calculated results show that efficient IR tunability can be achieved when the incident angle is below 50°. In the high ε state, the high spectral ***ε*** of the regulator will be maintained at large angles ranges covering between 0° and 50°, which is a desirable performance in maximizing the cooling power in hot weather[5]. After actuation, a low ***ε*** also can be maintained at large angles. The broadband IR tunability is better than that of ultra-broadband.

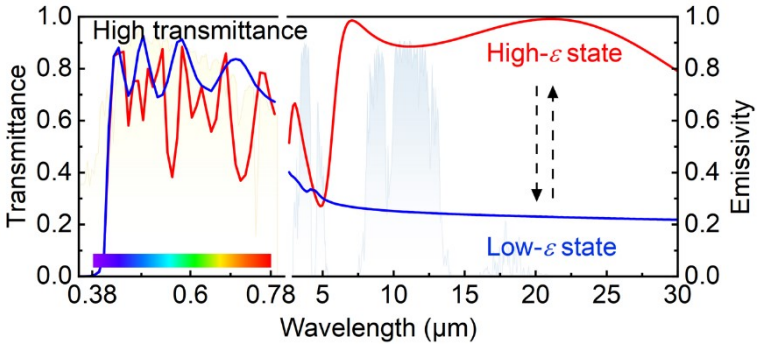

Fig. S5. Optimized spectra of IDIR regulator in high and low ε states aimed at maximizing $\triangle\varepsilon_{3\text{-}30\ \mu m}$. The size of g = 0.82 μm, and the other dimensions are the same as those of the sample aimed at maximizing $\triangle\varepsilon_{8\text{-}13\ \mu m}$. It shows that the $\varepsilon_{3\text{-}30\ \mu m}$ varies from 0.87 to 0.25 and $\triangle\varepsilon_{8\text{-}13\ \mu m}$ varies from 0.90 to 0.25 after actuation. It also shows a high VIS transmittance of 0.61 and 0.72 before and after actuation, respectively.

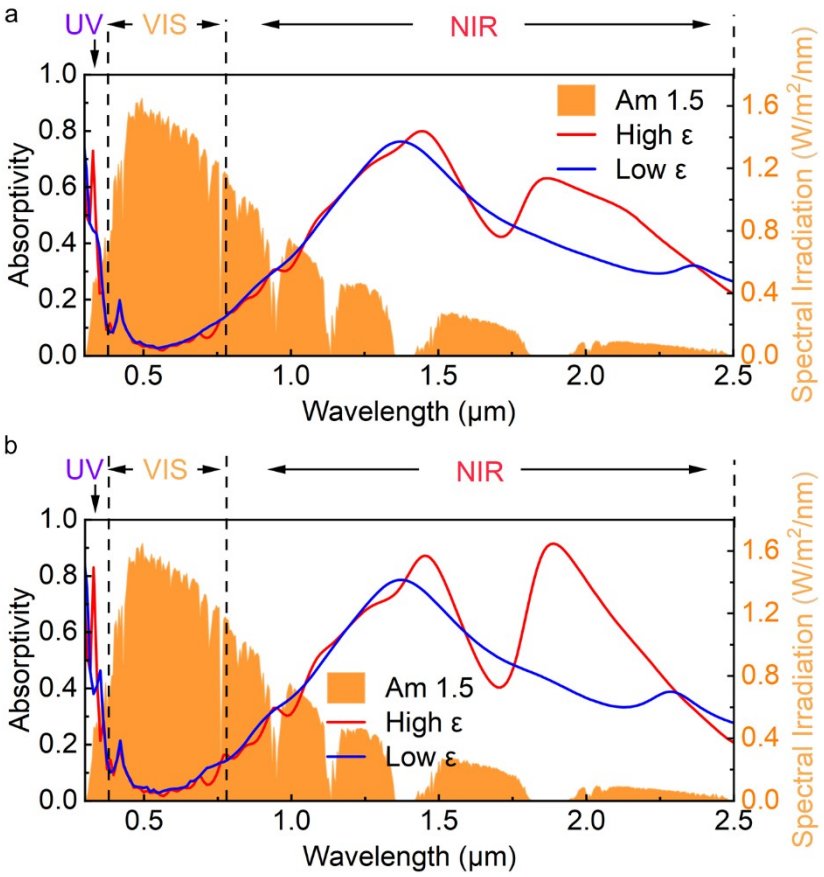

Fig. S6. Simulated absorptivity spectra of the IDIR regulator in the solar spectrum aimed to maximize (a) $\triangle\varepsilon_{8\text{-}13\ \mu m}$ and (b) $\triangle\varepsilon_{3\text{-}30\ \mu m}$. Air mass (AM) 1.5 direct solar spectrum (highlighted in orange). When aimed at maximizing $\triangle\varepsilon_{8\text{-}13\ \mu m}$, the IDIR regulator shows integrated solar irradiance absorptances α_{sun} of 0.219 and 0.220 in the high and low ε states, respectively. When aimed to maximize $\triangle\varepsilon_{3\text{-}30\ \mu m}$, the IDIR regulator shows integrated solar irradiance absorptance α_{sun} of 0.227 and 0.231 in the high and low ε states, respectively.

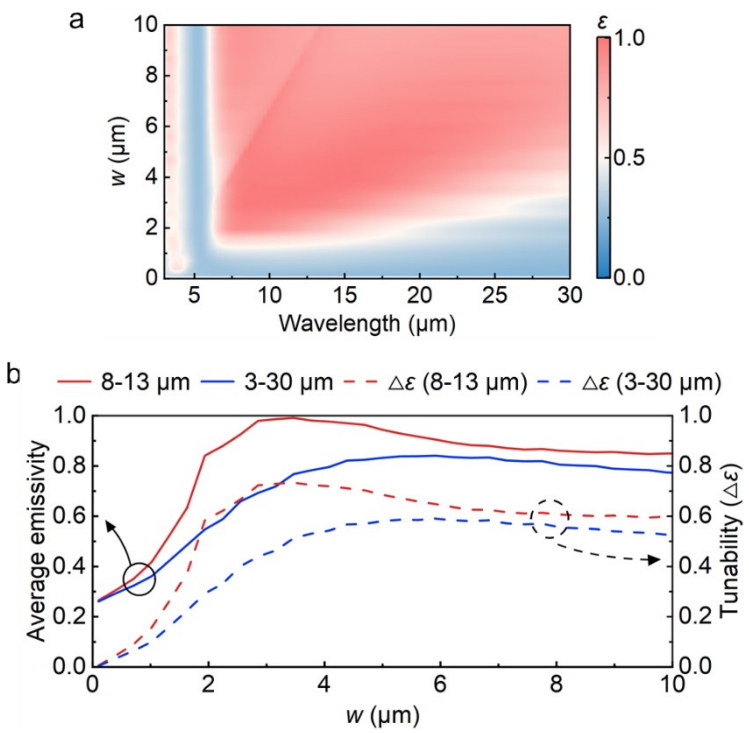

Fig. S7. Spectral ε as a function of w and wavelength in the 3-30 μm range. The average spectral $\triangle\varepsilon$ and tunability $\triangle\varepsilon$ as a function of w. The results show that $\triangle\varepsilon_{8\text{-}13\ \mu m}$ is always larger than $\triangle\varepsilon_{3\text{-}30\ \mu m}$, regardless of the increased w. When the value of w increases to 3.24 μm, the $\varepsilon_{8\text{-}13\ \mu m}$ and $\triangle\varepsilon_{8\text{-}13\ \mu m}$ reach maxima of 0.99 and 0.73 respectively.

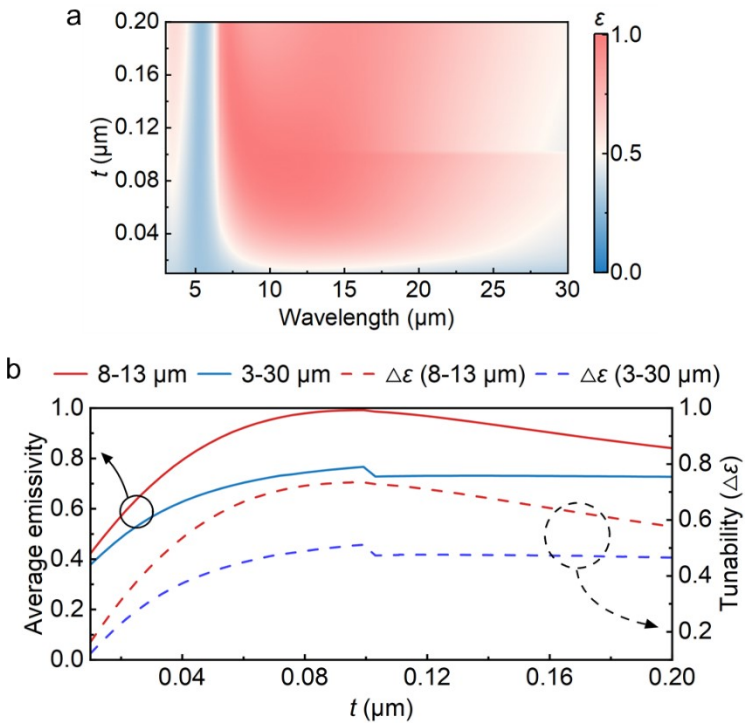

Fig. S8. Spectral ε as a function of t and wavelength in the 3-30 μm range. The average spectral ε and tunability $\triangle\varepsilon$ as a function of t. The results show that $\triangle\varepsilon_{8\text{-}13\ \mu m}$ is always larger than $\triangle\varepsilon_{3\text{-}30\ \mu m}$, regardless of the increased t. The results show that $\triangle\varepsilon_{8\text{-}13\ \mu m}$ is always larger than $\triangle\varepsilon_{3\text{-}30\ \mu m}$, regardless of the increased t and the optimal size of t = 0.1 μm.

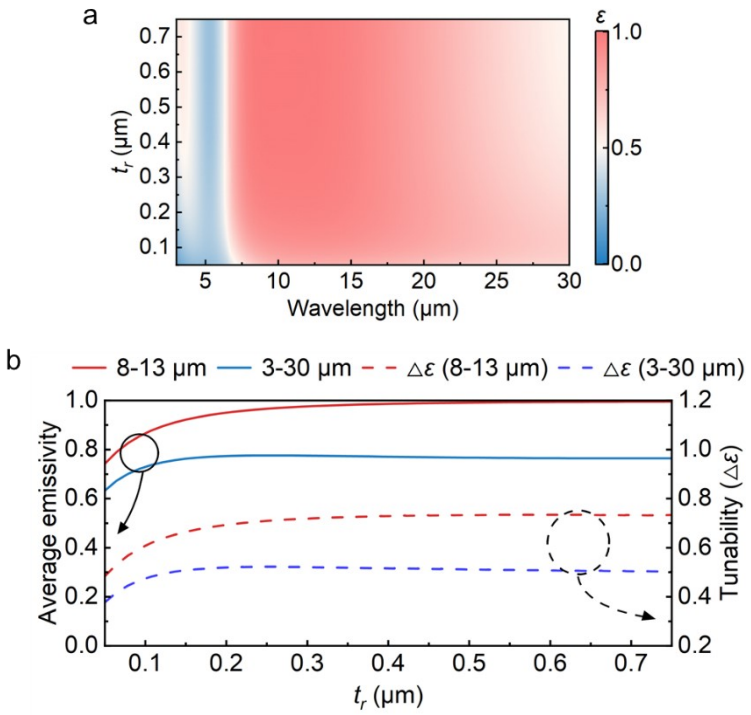

Fig. S9. Spectral ε as a function of t_r and wavelength in the 3-30 μm range. Average spectral emissivity and tunability $\triangle\varepsilon$ as a function of t_r. The results show that $\triangle\varepsilon_{8\text{-}13\ \mu m}$ is always larger than $\triangle\varepsilon_{3\text{-}30\ \mu m}$, regardless of the increased t_r and all the values of average spectral emissivity and tunability remain nearly constant after $t_r \geqq 0.5$ μm.

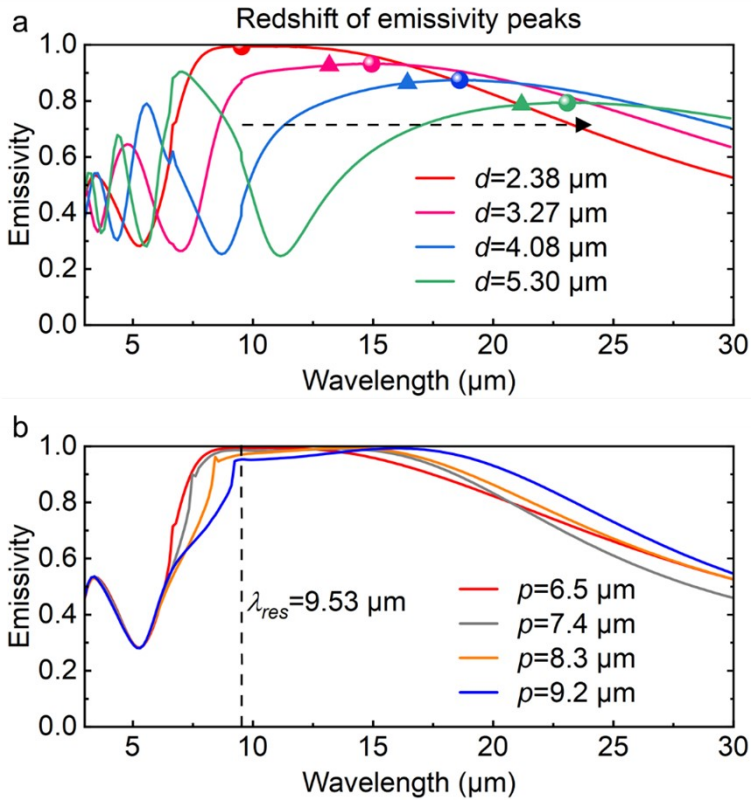

Fig. S10. Simulated absorption spectra of the IDIR regulator with different (a) dielectric thicknesses (*d*) and (b) periods (*p*) in the high *ε* state. (a) The F-P response wavelength (λ_{res}) calculated by $\lambda_{res} = \frac{4n_a d}{m}$ is marked with a solid triangle symbol. The simulated emittance peak is marked with the solid circle symbol. When *d* = 2.38 μm, F-P response peaks coincide with emittance peaks at the wavelength of 9.53 μm. (b) The period is given by *p* = *w*+*g*. The values of *p* were set to 6.5 μm (*w* = 3.24 μm, *g* = 3.27 μm), 7.4 μm (*w* = 3.68 μm, *g* = 3.71 μm), 8.3 μm (*w* = 4.13 μm, *g* = 4.16 μm), and 9.2 μm (*w* = 4.57 μm, *g* = 4.60 μm). The results show that adding the thickness of the dielectric cavity increases the resonant wavelength leading to the redshift of emissivity peaks. In addition, the emittance peaks dominated by F-P and SPPs response can be separated. However, adding the value of the period provides only a slight change in the resonant wavelength. Therefore, the emittance peaks dominated by F-P resonance are sensitive to the thickness and not very sensitive to the period.

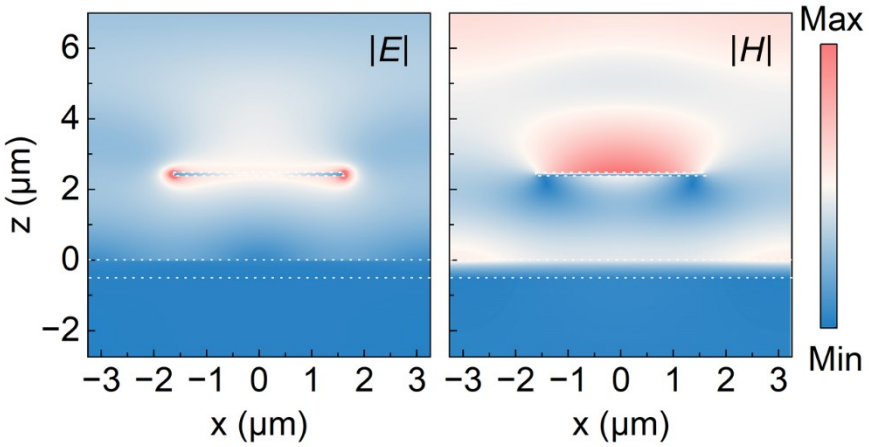

Fig. S11. Steady-state electromagnetic field distributions at the resonant wavelength of 9.53 μm in the high ε state. The electric and magnetic field distribution shows that the light is coupled into the air-slot and localizes around the metal corners between adjacent unit cells, creating an SPP-induced light absorption. The magnetic field distribution shows that PSP resonance exists in the dielectric layer.

References

1. Y.-W. Huang, H. W. H. Lee, R. Sokhoyan, R. A. Pala, K. Thyagarajan, S. Han, D. P. Tsai and H. A. Atwater, *Nano Letters*, 2016, **16**, 5319-5325.
2. Z. J. Coppens and J. G. Valentine, *Adv Mater*, 2017, **29**.
3. M. Chen, X. Zhang, D. Yan, J. Deng, W. Sun, Z. Li, Y. Xiao, Z. Ding, J. Zhao and Y. Li, *Materials Horizons*, 2023, **10**, 2191-2203.
4. F. Lai, L. Lin, R. Gai, Y. Lin and Z. Huang, *Thin Solid Films*, 2007, **515**, 7387-7392.
5. D. Wu, C. Liu, Z. Xu, Y. Liu, Z. Yu, L. Yu, L. Chen, R. Li, R. Ma and H. Ye, *Materials & Design*, 2018, **139**, 104-111.